Towards Analytical Modeling of Tonal and Broadband Sources of Axial Fan Noise

Towards analytical modeling of tonal and broadband sources of axial fan noise

Francesco Bellelli[1], Renzo Arina[1], Stéphane Moreau[2], and Francesco Avallone[1]
[1]*Department of Mechanical and Aerospace Engineering, Politecnico di Torino, Torino, 10129, Italy*
[2]*Department of Mechanical Engineering, Université de Sherbrooke, Sherbrooke, Québec, Canada*

This work presents an analytical model for predicting tonal and broadband noise in low-speed axial fans coupled with of a statoric shroud. The model accounts for all the main dipolar noise sources, including unsteady loading tonal noise on both rotor and stator, trailing-edge broadband noise from boundary layer scattering on both rotor and stator, and leading-edge broadband noise from wake impingement on the stator. The mean blade loading is obtained through a modified blade element momentum theory, while the unsteady loading fluctuations are computed using an extended Sears' model coupled with potential flow theory. Broadband contributions are evaluated using Amiet's formulation for trailing-edge and leading-edge noise, including back-scattering corrections. The proposed approach is validated against high-fidelity lattice-Boltzmann simulations for two fan configurations, one with evenly spaced blades and vanes and one with random uneven spacing of blades and vanes, at both free blowing and maximum efficiency operating conditions. The model predicts well the mean aerodynamic loading, tonal components, and spectral variations induced by uneven spacing, while broadband noise levels are well captured except for underestimation at operating conditions where the tip vortex backflow dominates. Overall, the framework provides a computationally efficient tool for fan noise prediction and design optimization, bridging the gap between high-fidelity simulations and early stage analytical design.

I. Nomenclature

B, V	=	Number of rotor blades and stator vanes [-]
x, y, z	=	Axial, horizontal, and vertical coordinates [m]
$r = \sqrt{y^2 + z^2}$	=	Radial position in the $x = 0$ plane [m]
$\theta = \tan^{-1}(y/z)$	=	Azimuthal position in the $x = 0$ plane [°]
c	=	Fan tip chord [m]
t_c	=	Fan tip clearance [m]
s	=	Rotor-stator axial separation [m]
γ	=	Twist/stagger angle [°]
v	=	Upwash velocity [m/s]
Ω	=	Fan rotational frequency [Hz]
p	=	Static pressure [Pa]
ρ	=	Density [kg/m^3]
ν	=	Kinematic viscosity [m^{2}s]
T	=	Fan thrust [N]
Q	=	Fan aerodynamic torque [Nm]
c_0	=	Sound speed [m/s]
f	=	Frequency [Hz]
N_s, N_c	=	Number of spanwise and chordwise points [-]
D, D_h	=	Fan tip and hub diameters [m]
$R = D/2, R_h = D_h/2$	=	Fan tip and hub radii [m]
u, v_r, v_θ	=	Axial, radial, and tangential velocity components [m/s]
$v_{tip} = \Omega R$	=	Tip velocity [m/s]
$\Delta p = p_{amb} - p$	=	Fan pressure rise [Pa]

$\dot{V}$	=	Volume flow rate through the fan [m^3/s]
$\Psi = 2\Delta p/\rho v_{tip}^2$	=	Pressure rise coefficient [-]
$\varphi = 4\dot{V}/\pi(D^2 - D_{hub}^2)v_{tip}$	=	Flow coefficient [-]
$Re_c = v_{tip}c/\nu$	=	Reynolds number based on the chord at the tip [-]
BPF = $B\Omega$	=	Blade Passing Frequency [Hz]
SPL = $20\log_{10}\left(p_{rms}/2\cdot 10^{-5}\right)$	=	Sound Pressure Level [dB/Hz]
OASPL = $10\log_{10}\left(\sum_i 10^{SPL(f_i)/10}\right)$	=	Overall Sound Pressure Level [dB/Hz]

II. Introduction

Fan noise is critical for manufacturers because of more stringent requests due to annoyance. For this reason, it is necessary to simultaneously optimize aerodynamic and aeroacoustics performance in the early stages of design. However, high-fidelity Computational Fluid Dynamics (CFD) simulations are often too computationally expensive in the design phase. Therefore, analytical and low-fidelity models are crucial to ensure an efficient and rapid design process [1].

Several noise sources are present in a cooling fan. Monopole (thickness) noise source is caused by the air displacement due to the blade passage and is usally not dominant at low Mach number [2]. Quadrupole noise source is instead caused purely by the turbulent flow field and is also considered negligigble at low Mach number [3]. Finally, dipole (loading) noise source is caused by the force acting on lifting surfaces. Loading noise can be split into steady and unsteady loading noise. The former characterizes the noise spectrum with narrowband peaks at frequencies multiple of the Blade Passing Frequency (BPF), defined as $BPF = \Omega B$, in the hypothesis of azimuthally evenly spaced blades. If the blades are not evenly spaced, additional peaks at subharmonic frequencies are present. Sharland [3] showed that, when present, the unsteady component of loading noise outweights the steady one.

A source of blade loading fluctuation is the rotation of the blades in a non-uniform inflow. This results in narrowband peaks at the BPF and harmonics, as well as at subharmonic frequencies, in the far-field noise spectrum, depending on the periodicity of the flow distortions. For example, the flow distortions can be caused by the viscous wake shed by the rotor blades on the stator vanes, or by the non-viscous potential effect of the stator vanes on the rotor blades [4]. Vella et al. [5] used potential flow theory, to model the flow field near the blade, combined with Sears' model [6] for unsteady blade loading and Hanson model [7] for far-field noise propagation, leading to sufficiently fast and accurate acoustic results. Sanjosé et al. [8, 9] computed the rotor-stator potential interaction noise on the NASA ANCF rig using Parry's model [10] to obtain the unsteady blade loading and the potential flow theory to compute the flow field at the trailing-edge of the blades. Results were well aligned with high fidelity numerical simulations, proving that the implied potential flow theory is sufficient to predict the potential excitation of the stator vanes seen by the rotor blades.

When a turbulent flow impinges on the blades, additional loading fluctuations are present, causing the so-called turbulent ingestion noise. It is typically dominant at low frequency and contributes to both the broadband and tonal noise, depending on the topology of the turbulent structures. Sanjosé and Moreau [11] used an approach based on Amiet leading-edge noise model [12] to compute the turbulent ingestion noise of an axial fan. They fed the model with isotropic von Kàrmàn and Liepmann turbulence spectra computed with the aid of RANS simulations and were able to obtain accurate results at low fan flow rates up to the design point, while consistently underestimating the total Sound Power Level (SWL) at higher flow rates. Dieste and Gabard [13] used instead a Random Particle Mesh (RPM) method to generate a synthetic turbulent field that includes non-Gaussian filters to include more realistic energy spectra. They validated their work against the conventional Amiet [12] formulation and obtained encouraging results on the prediction of turbulence energy spectra.

The scattering of the boundary layer at the blade trailing-edge produces an additional noise source that is usually dominant at medium and high frequencies, as demonstrated by Caro and Moreau [14]. Sanjosé and Moreau [11] applied Amiet model [12], fed with RANS-extracted boundary layer parameters to an automotive engine cooling fan, proving the feasibility of trailing-edge noise prediction on complex geometries. Later, Coutty and Moreau [15] applied the same methodology to a more complex full engine cooling module, leading to promising results. Finally, Arroyo Ramo et al. [16] proposed a novel data-driven approach to compute the wall pressure spectra used to feed Amiet model. They found that, using Artificial Neural Networks (ANN), it is possible to describe the boundary layer with three parameters and also to predict the wall pressure spectra within 3 dB/Hz for any type of pressure gradient to which the airfoil is subjected to.

While numerous studies on axial fan noise prediction have developed sophisticated models tailored to specific noise sources, they typically focus on isolated contributions, requiring distinct physical assumptions, measurement inputs, and computational strategies for each case. This fragmentation not only complicates the early stage design process but limits

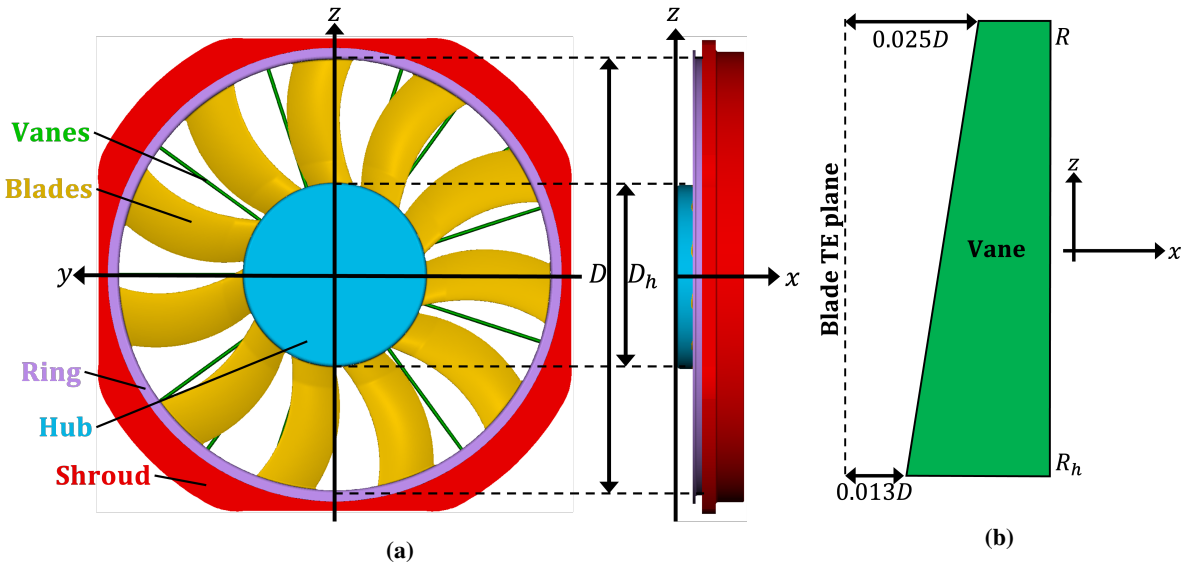

Fig. 1 Reference engine cooling fan. The main parts of the system are shown with different colors. (a): Cooling fan. (b): Sketch of a stator vane at $y/D = 0$.

the ability to systematically assess interactions between multiple noise sources or leverage shared aerodynamic inputs across calculations. There remains a gap for unified analytical approaches that can consistently incorporate a broad range of both tonal and broadband noise generation mechanisms within the same computational workflow and using consistent aerodynamic inputs.

This paper proposes an analytical model for fan noise prediction that considers both rotor and stator loading noise and that includes all the main noise sources of engine cooling fans coupled with a statoric shroud. They include the unsteady loading tonal noise on the rotor blades induced by the presence of the stator vanes downstream, the unsteady loading tonal noise on the stator vanes induced by the impinging wake shed by the rotor blades, broadband trailing-edge noise resulting from the scattering of the turbulent boundary layer at the trailing-edge of both rotor and stator, and the broadband leading-edge noise resulting from the impingement on the stator vanes of the wake shed by the rotor blades. This versatility enables simultaneous consideration of interdependent noise sources, streamlines model validation, and enhances the utility of low-fidelity fan noise prediction tools for parametric optimization.

The remainder of the paper is structured as follows: Section III describes the reference fan geometry and Section IV details the analytical model. Section V describes the numerical setup used for validation against high-fidelity CFD simulations, while the results obtained are discussed in Section VI. Finally, the main conclusions are presented in Section VII.

III. Reference geometry

The reference fan geometry consists of a rotor and a stator, as shown in Fig. 1a. The rotor has $B = 11$ identical blades connected to a hub at the root and to a ring at the tip. The rotor diameter is $D = 0.465$ m and the hub-tip ratio is $D_h/D = 0.42$. The chord at the tip is $c/D = 0.14$ and the tip clearance is $t_c/D = 0.0086$. The rotor blades are swept in the yz plane, as visible in Fig. 1a. The stator has $V = 20$ identical vanes connected to a shroud. The stator vanes are skewed in the xz plane, as shown in Fig. 1b. This changes the rotor-stator axial separation from $s/D = 0.013$ at the hub to $s/D = 0.025$ at the tip. It should be noted that the vane skew is obtained by decreasing the vane chord from the hub to the tip, while keeping fixed the trailing-edge position along the x axis. The present geometry is a simplified version of the one described by the autors in [17].

In order to assess the model capability to predict the SPL variations at discrete frequencies, two different configurations have been tested. The first configuration (EB/EV) is characterized by an even azimuthal spacing of both blades and vanes, while the second configuration (UB/UV) is characterized by an uneven azimuthal spacing of both blades and vanes at the hub. The UB/UV configuration has been obtained by randomly perturbating the angular position of blades and vanes, bounded between 25% and 140% of the EB/EV configuration, with an approach similar to the one described

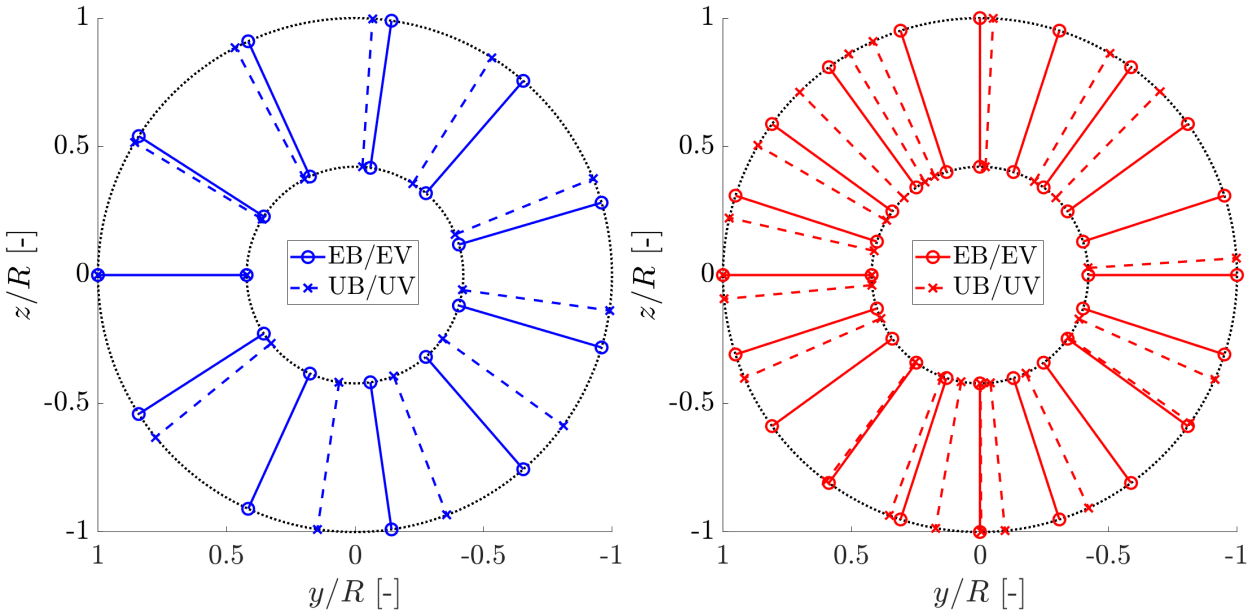

Fig. 2 Sketch of the angular position of the EB/EV and UB/UV configurations in the yz plane. (a): Rotor blades. (b): Stator vanes.

	Ψ	φ	Ω	Re_c
Free blowing	0	0.19	50.8 Hz	$3.2 \cdot 10^5$
Max efficiency	0.14	0.10	50.8 Hz	$3.2 \cdot 10^5$

Table 1 Summary of the key parameters at the two tested operating conditions.

by Cattanei et al. [18]. A schematic representation of the azimuthal distribution of rotor blades and stator vanes for the two configurations is provided in Figs. 2a and 2b.

The fan has been tested at both free blowing ($\Psi = 0$), and maximum efficiency ($\Psi > 0$) conditions at a rotational speed of the fan $\Omega = 50.8$ Hz. A summary of the key parameters at these two operating points is provided in Tab. 1.

IV. Methodology

A flowchart of the model implementation is depicted in Fig. 3. The model has been implemented in MATLAB and run on an Intel i9-10900X 4.50 GHz Dell Precision 5820 X-Series workstation. The average computational cost is 0.02 CPU hours.

The model considers several noise contribution from the fan system. Specifically, it models both rotor and stator dipolar noise contributions. Each contribution is composed by tonal and a broadband components. The tonal part accounts for the unsteady loading noise and, only for the rotor, also for the steady loading noise. The broadband part accounts for the trailing-edge noise and the leading-edge noise, respectively coming from the scattering of the turbulent boundary layer at the trailing-edge and the incoming turbulent field at the leading-edge.

The tonal part for the sole rotor surface contribution at free blowing has been already validated in a previous work by the authors [19].

A. Tonal noise

Each blade is discretized in N_s points in the spanwise direction and N_c points in the chordwise direction. The values for N_s and N_c are chosen so that the resulting length of each spanwise and chordwise segment is acoustically compact in the frequency range of $0 \leq f/BPF \leq 4$. For each spanwise position r, the chord $c(r)$ and twist $\gamma(r)$ as well as the

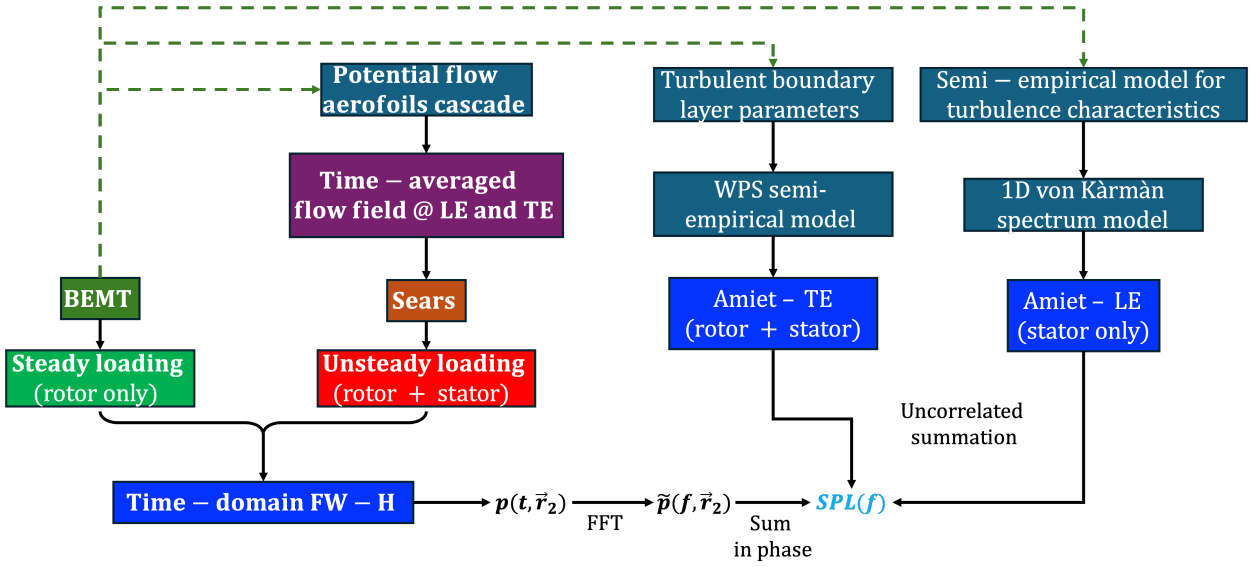

Fig. 3 Flowchart of the model.

sectional airfoil shape (thickness and camber), the segment azimuthal phase, and the rotor to stator axial spacing are extracted from the CAD model.

Each segment is modelled as a compact dipole and the resulting noise at a probe located at $\vec{r}_1 = \{x, y, z\}$ in the far-field is calculated by means of the Ffowcs Williams and Hawkings (FWH) acoustic analogy in the time domain [20–22]. Following the reference frame sketched in Fig. 4, the acoustic pressure at an observer time t produced by a rotating compact dipole located at a distance $\vec{r}_2 = \{x, y - r\cos\theta, -r\sin\theta\}$ with respect to the far-field probe is calculated as

$$p(\vec{r}_2, t) = \frac{\vec{r}_2}{4\pi c_0 r^2 (1 + M_r)^2} \cdot \left(\frac{\partial \vec{F}}{\partial \tau} + \frac{\vec{F}}{1 - M_r} \frac{\partial M_r}{\partial \tau} \right), \tag{1}$$

where $M_r = My\sin\theta$ is the convective amplification term, $M = \Omega r / c_0$ is the Mach number, and $\vec{F} = \{T, D, L\}$ is the vector containing the axial, tangential and radial components of the force. For low-speed axial fans, the radial component can be neglected [20]. The force and the convective Mach number derivatives are computed with respect to the emission time $\tau = t - ||\vec{r}_2||/c_0$. The acoustic pressure resulting from each rotating dipole is first converted in the frequency domain and, then, all the contributions from the dipoles are summed accounting for the source phase angle. For the stator noise contribution, only the loading derivative term is non-zero, leading to a simplified equation that is omitted for brevity.

The mean value of the force acting on each spanwise strip only on the rotor is computed by means of the Blade Element Momentum Theory (BEMT), assuming a uniform axial inflow with velocity V_∞. A sketch of the generic blade section is provided in Fig. 5. For each spanwise position r, the sectional thrust and torque are calculated following both the momentum theory and the blade element theory. To include the possibility of having a non-zero pressure rise Δp, the momentum balance equation along the x axis is modified, leading to the following two equations:

$$\begin{cases} \dfrac{dT}{dr} = (2\pi r - \Delta p)\left[2r\rho V_\infty^2 (1 + a)a\right] = B\dfrac{1}{2}\rho V_1^2 c(c_l\cos\phi - c_d\sin\phi), \\ \dfrac{dQ}{dr} = 4\pi r^2 \rho V_\infty^2 \Omega r(1 + a)b = B\dfrac{1}{2}\rho V_1^2 c(c_l\sin\phi + c_d\cos\phi)r, \end{cases} \tag{2}$$

where $a = u/V_\infty - 1$ is the axial velocity induction coefficient, $b = 1 - v_t/(\Omega r)$ is the tangential velocity induction coefficient, $\phi = \gamma - \alpha$ is the inflow angle, α is the angle of attack to which the blade section is subject, and $V_1 = \sqrt{u^2 + v_t^2}$ is the total velocity at each radial section. The lift coefficient $c_l(\alpha, Re_c, M)$ and drag coefficient $c_d(\alpha, Re_c, M)$ of the sectional airfoil are calculated by interpolating a predefined polar database, which is computed by means of the XFOIL

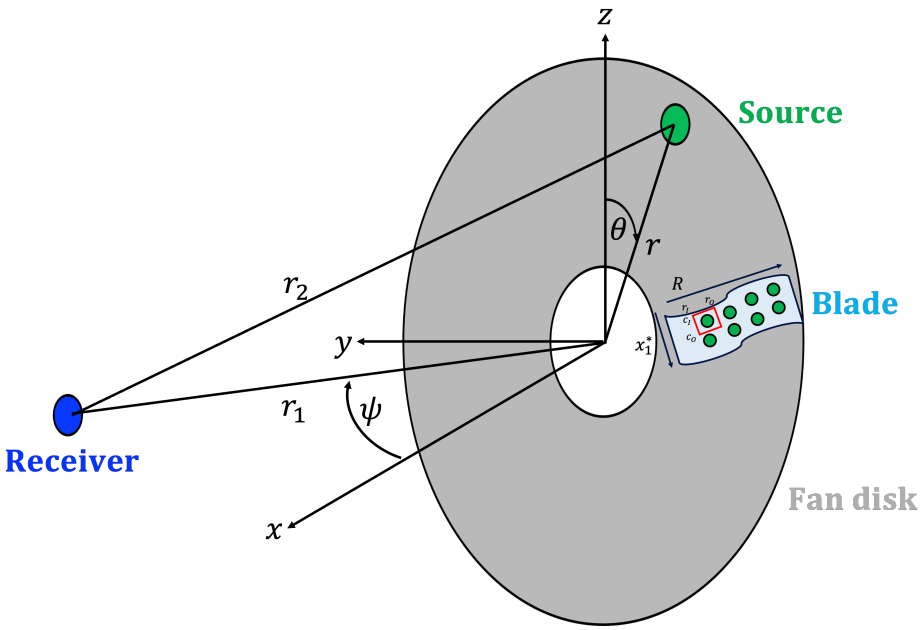

Fig. 4 Schematic view of the noise calculation and of the blade discretization for the tonal noise calculation.

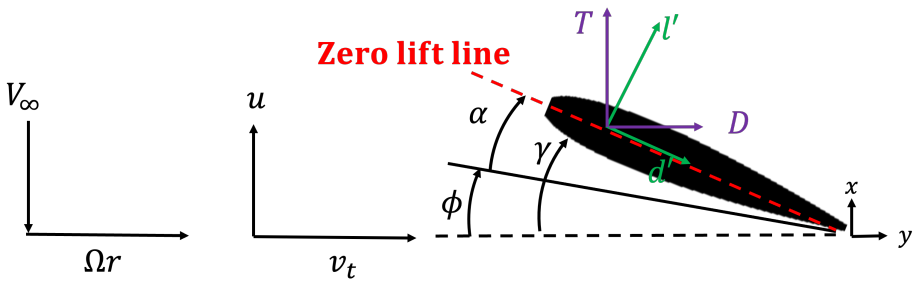

Fig. 5 Schematic view of the generic blade section used in the BEMT calculation.

tool [23]. Starting from a tentative value, the axial and tangential velocity induction factors are calculated from Eq. 2 and iteratively updated until convergence. The Prandtl-Glauert compressibility correction factor

$$C = \frac{1}{\sqrt{1-M^2} - \dfrac{M^2}{1+\sqrt{1-M^2}}\dfrac{||c_l||}{2}}, \tag{3}$$

is applied to the lift coefficient c_l, while the hub and tip losses are considered by introducing the correction factor

$$F = \left(\frac{2}{\pi}\right)^2 \exp\left(-\frac{B}{2}\sqrt{1+\left(\frac{\Omega r^2}{V_\infty(1+a)}\right)^2}\frac{R-R_h}{r}\right). \tag{4}$$

The unsteady component of the force acting on each strip at a frequency $f = w\Omega$, with $w \in \mathbb{Z}$, is computed with the Sears' model [6] as

$$\tilde{F}(w, x_1^*, r) = \iint c(r)\rho\Omega r\tilde{v}(w, r)S(w)\sqrt{\frac{1-x_1^*}{1+x_1^*}}dx_1^* dr, \tag{5}$$

where $c(r)$ is the chord at the spanwise location r, ρ is the air density, $\tilde{v}(w, r)$ is the azimuthal Fourier transform of the upwash velocity at a frequency f and spanwise position r, $x_1^* = 2x_1/c - 1$ is the non-dimensional chordwise coordinate, x_1 is the chordwise coordinate on the airfoil, and $S(w)$ is the Sears' transfer function. To improve the accuracy of the Sears' model, Eq. 5 is expanded to consider compressibility effects [24] as well as angle of attack and camber [25, 26]. Equation 5 is fed with the time-averaged flow field of the upwash velocity component sampled at the blade trailing-edge and vane leading-edge, which provide information on the rotor-stator potential interaction on both rotor and stator surfaces. To use the Sears' model for computing the downstream rotor-stator interaction, the reversed Sears' approach [27] is utilized, similarly to what has been done by Vella et al. [5].

The 2D inviscid velocity field in the vicinity of an infinite aerofoils cascade is computed as proposed by Baddoo et al. [28] and is used as input to Sears' model in Eq. 5. Therefore, the complex velocity Φ is defined as

$$\begin{aligned}\Phi(z) =& \mathrm{i}\alpha\left(1-\exp\left(\frac{-\pi}{d}\right)\sqrt{\frac{\sinh\left(\pi\dfrac{z-\exp(\mathrm{i}\gamma)}{d}\right)}{\sinh\left(\pi\dfrac{z+\exp(\mathrm{i}\gamma)}{d}\right)}}\right) - \frac{1}{d}\int_{-1}^{1} y'_{\mathrm{th,v}}(\tau)\coth\left(\frac{\pi\left(\tau\exp(\mathrm{i}\gamma)-z\right)}{d}\right)\exp(\mathrm{i}\gamma)\,\mathrm{d}\tau \\ &- \frac{1}{\mathrm{i}}\sqrt{\frac{\sinh\left(\pi\dfrac{z-\exp(\mathrm{i}\gamma)}{d}\right)}{\sinh\left(\pi\dfrac{z+\exp(\mathrm{i}\gamma)}{d}\right)}}\int_{-1}^{1} y'_{\mathrm{c,v}}(\tau)\sqrt{\frac{\sinh\dfrac{\exp(\mathrm{i}\gamma)\pi(1+\tau)}{d}}{\sinh\dfrac{\exp(\mathrm{i}\gamma)\pi(1-\tau)}{d}}}\left(\coth\left(\frac{\pi\left(\tau\exp(\mathrm{i}\gamma)-z\right)}{d}\right)-1\right)\exp(\mathrm{i}\gamma)\,\mathrm{d}\tau,\end{aligned} \tag{6}$$

where the prime notation means a differentation with respect to the chordwise coordinate x_1^*, $y_{c,v}$ represents the camber distribution, and d the separation between two consecutive aerofoils in the infinite cascade. The resulting equation is solved at each spanwise location r and the resulting flow field is calculated at a distance s from the cascade leading-edge or trailing-edge, depending on the noise contribution that is being calculated. Specifically, the flow field at a distance s from the cascade leading-edge is used to compute the loading harmonics on the rotor blades caused by the potential interaction with the stator vanes, while the flow field at a distance s from the cascade trailing-edge is used to compute the loading harmonics on the stator vanes caused by the impingement of the wake shed by the rotor blades. To consider the possibility of having an uneven azimuthal distribution of the aerofoils, such as in the UB/UV configuration, the flow field is extracted in the interstage between two consecutive ones and stitched together after repeating this procedure for all the consecutive couples.

B. Broadband noise

The rotor and stator broadband noise contributions are calculated by coupling the Blade Element Theory (BET) with Amiet's theory for leading-edge and trailing-edge noise, including the trailing-edge and leading-edge back-scattering terms respectively, as proposed by Roger and Moreau [29]. Even though both formulations can be applied almost

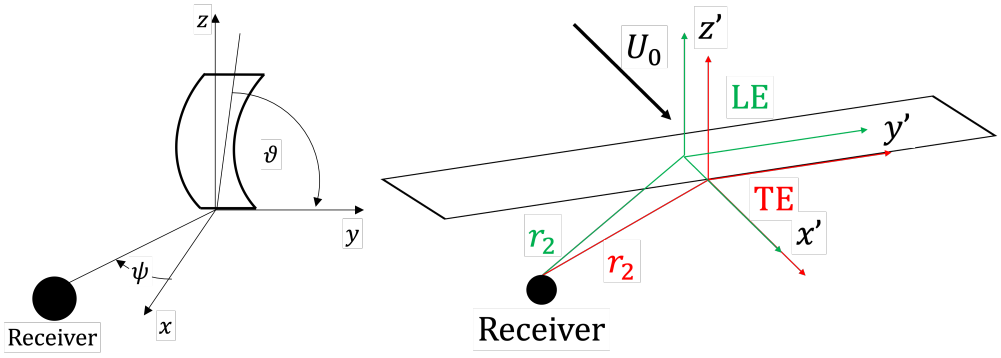

Fig. 6 Sketch of the geometrical configuration for leading-edge and trailing-edge noise calculations. (a): Sketch of the listener location with respect to the blade planform in the disk plane. (b): Sketch of the spanwise strip and the reference frames. The span is along y' while the chord is along x'.

identically to rotor and stator surfaces, the leading-edge noise model has been applied only to the stator surface. The reason behind this choice is that high intensity turbulence is not present upstream of the rotor since the simulations have been carried out in a free-field environment. Both leading-edge and trailing-edge noise models of Amiet's theory share a common mathematical basis, which is briefly outlined in the following. Figure 6 sketches the main geometrical parameters used in the model description.

Let $S_{pp}(\omega, \vec{r}_2)$ be the Power Spectral Density (PSD) of far-field acoustic pressure emitted by each spanwise strip located at $\vec{r}_2$ with respect to the listener, at the angular frequency $\omega = 2\pi f$. This term has to be properly summed to consider the contribution of each spanwise strip of each blade/vane. The main assumption is that each signal $S_{pp,i}(\omega, \vec{r}_2)$ is uncorrelated from the others, so a simple algebraic summation is carried out. Therefore, if the considered surface is the stator one, the PSD of far-field acoustics of the whole stator is computed simply as

$$S(\omega) = V \sum_{i=1}^{N_s} S_{pp,i}(\omega, \vec{r}_2) \tag{7}$$

since no Doppler effect is present in the case of a stationary source.

When considering the rotor surface contribution, the PSD of far-field acoustic pressure of each spanwise strip is summed considering the approach of Sinayoko et al. [30, 31] as follows. Given the emitted frequency

$$\omega_e(\omega, \vec{r}_2) = \omega(1 + M \sin\psi \sin\theta), \tag{8}$$

the PSD of far-field acoustic pressure of the whole rotor is computed as

$$S(\omega) = \sum_{i=1}^{N_s} \frac{B}{2\pi} \int_0^{2\pi} \left(\frac{\omega_e}{\omega}\right)^2 S_{pp,i}(\omega_e, \vec{r}_2) d\theta. \tag{9}$$

Finally, the PSD is converted into SPL in dB as

$$SPL(f) = 10 \log_{10} \left[\frac{2\pi S(f) \Delta f}{p_{ref}^2} \right], \tag{10}$$

where Δf is the frequency resolution and $p_{ref} = 2 \cdot 10{-}5$ Pa is the reference pressure.

1. Trailing-edge noise

The PSD of far-field acoustic pressure emitted by each spanwise strip of length L is given by

$$S_{pp}^{(TE)}(\omega, \vec{r}_2) = 2 \left(\frac{\omega z c}{4\pi c_0 \sigma_0} \right)^2 L |\mathcal{L}|^2 \Phi_{pp}^{(TE)}(\omega) l_y(\omega), \tag{11}$$

where $\vec{r}_2$ is the distance between the trailing-edge of the strip and the observer, $\sigma_0 = \sqrt{x'^2 + \beta^2(y'^2 + z'^2)}$, and $\beta = \sqrt{1 - M^2}$. The radiation integral $\mathcal{L}$ is computed following the approach proposed by Roger and Moreau [29] that considers also the back-scattering of the leading-edge, a relevant term at low frequency.

The wall pressure spectrum $\Phi_{pp}^{(TE)}(\omega)$ is computed at the Suction Side (SS) and Pressure Side (PS) using two different semi-empirical models that can be expressed in the following general form

$$\Phi_{pp}^{(TE)}(\omega) = \frac{1}{\mathcal{S}} \frac{a\,(\omega\mathcal{F})^b}{\left[i\,(\omega\mathcal{F})^c + d\right]^e + \left[\left(f R_T^g\right)(\omega\mathcal{F})\right]^h}, \tag{12}$$

where $\mathcal{S}$ is a spectral scaling term, $\mathcal{F}$ is a frequency scaling term, $R_T = (\delta/U_e)/(\nu/u_\tau)$ is the time-scales ratio, and a to h are coefficients that are calculated from the turbulent boundary layer parameters at the trailing-edge. In the literature, several models are available to prescribe such coefficients. At the SS, the Kamruzzaman's model [32] has been used, while at the PS the Goody's model [33] has been selected. The turbulent boundary layer parameters have been extracted at 97.5% of the chord for the SS and at the 95% of the chord for the PS using XFOIL. Since the boundary layer thickness δ is not provided by XFOIL, it has been computed as

$$\delta = \theta\left(3.15 + \frac{1 - 72}{H - 1}\right) + \delta^*, \tag{13}$$

where θ is the boundary layer momentum thickness and δ^* is the boundary layer displacement thickness. H is the ratio between δ^* and θ.

The spanwise correlation length $l_y(\omega)$ is computed using Corcos' model [34] as

$$l_y(\omega) = \frac{U_c}{b\omega}, \tag{14}$$

where $U_c = \alpha_1 U_0$ is the convection velocity and b is a parameter currently assumed unitary. The convection velocity ratio α_1 has been assumed equal to 0.7.

2. Leading-edge noise

The PSD of far-field acoustic pressure emitted by each spanwise strip of length L is given by

$$S_{pp}^{(LE)}(\omega, \vec{r}_2) = \left(\frac{\rho\omega z c}{2c_0\sigma_0}\right)^2 \pi U_0 L |\mathcal{L}|^2 \Phi_{pp}^{(LE)}(\omega), \tag{15}$$

where $\vec{r}_2$ in this case is the distance between the listener and the airfoil mid chord point.

The turbulence spectrum of the upwash velocity $\Phi_{pp}^{(LE)}(\omega)$ is computed using the one-dimensional von Kàrmàn spectrum [35]

$$\Phi_{pp}^{(LE)}(\omega) = \frac{1}{\sqrt{\pi}} \frac{\Gamma\left(\frac{5}{6}\right)}{\Gamma\left(\frac{1}{3}\right)} \frac{u_\sigma}{k_e} \frac{1}{\left(1 + \hat{k}_x^2\right)^{\frac{5}{6}}}, \tag{16}$$

where Γ is the Gamma function, $k_x = \omega/U_0$, u_σ is the velocity turbulent fluctuation, Λ_f is the integral length scale,

$$k_e = \frac{\sqrt{\pi}}{\Lambda_f} \frac{\Gamma\left(\frac{5}{6}\right)}{\Gamma\left(\frac{1}{3}\right)}, \tag{17}$$

and, finally, $\hat{k}_x = k_x/k_e$.

The one-dimensional von Kàrmàn spectrum is fed with u_σ and Λ_f computed with the semi-empirical model proposed by Meier and Moreau [36] to consider the rotor wake impingement on the stator vanes.

$$\begin{cases} Tu = \dfrac{u_\sigma}{U_0} = \sqrt{\left(\dfrac{K_{u,1} c B c_l}{4\pi r}\right)^2 + \left(0.9 K_{u,2} 0.24 Re^{\frac{-1}{10}}\right)^2}, \\ \\ \Lambda_f = K_l(\delta + as). \end{cases} \tag{18}$$

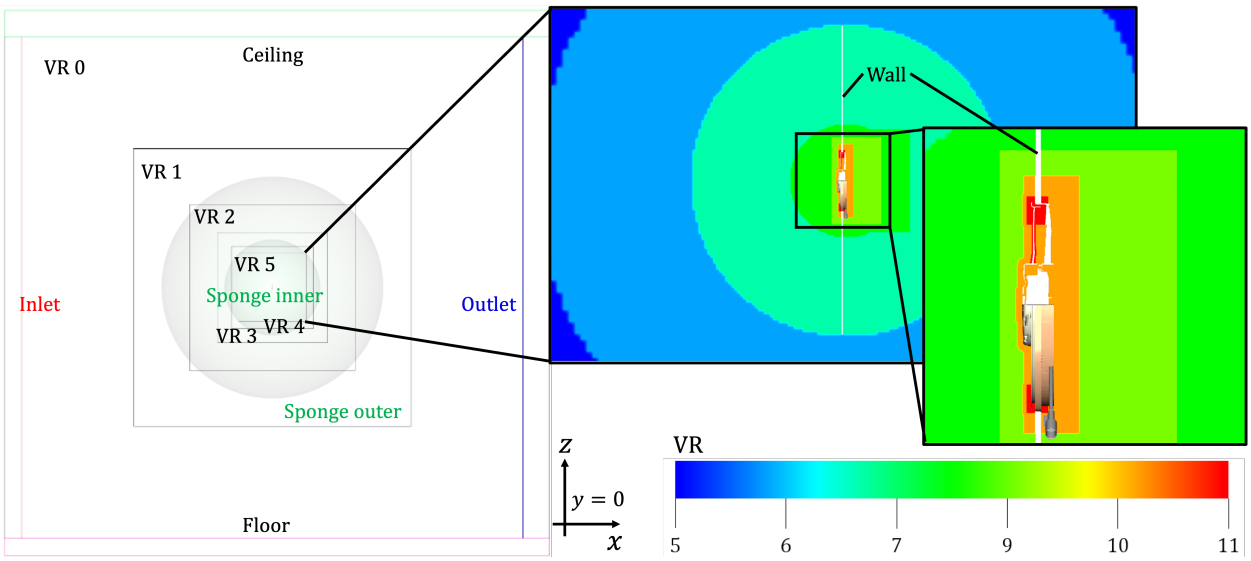

Fig. 7 Sketch of the computational domain in the plane at $y/D = 0$. The wall is used only at maximum efficiency.

The values of c_l and Re are the ones used for the BEMT calculation, the value of δ is the one used for the trailing-edge noise, and s is the rotor-stator axial spacing. The coefficients $K_{u,1}$, $K_{u,2}$, K_l, and a have been assumed equal to 0.3, 0.5, 1, and 0.04 respectively as suggested in the work of Meier and Moreau [36].

V. High-fidelity CFD simulation setup

High-fidelity CFD simulations based on the Lattice-Boltzmann Method (LBM) [37] have been used to validate the analytical model. They have been carried out using the commercial software PowerFLOW version 6 from 3DS. To reduce the computational cost, a Very Large Eddy Simulation (VLES) approach has been used, thus resolving only the largest turbulent scales. The subgrid model implemented in the software derives from the renormalization group $k-\epsilon$ transport equations (RNG $k-\epsilon$) [38]. The wall model used by PowerFLOW is the Pressure-Gradient Extended Wall Model (PGE-WM), which is an extension of the generalized wall model proposed by Launder and Spalding [39]. For more detail the reader is referred to [39, 40].

The computational domain is shown in Fig. 7. A large cubic fluid domain of side length equal to $135D$ has been built to simulate a free-field environment. The ceiling and the floor of the simulation domain have been modelled as a solid reflecting wall, while both inlet and outlet have been set as static pressure boundary conditions. A discretization strategy based on 11 Variable Resolution (VR) regions has been adopted. The regions with maximum resolutions have been set around the rotating blades and near the tip gap region to obtain 11 voxels in the tip clearance. The resolution in the tip gap region is similar to the one adopted by Avallone et al. [41]. The voxel size between one VR region and the adjacent one is doubled. A sponge region has been defined by an artificial change of viscosity of a factor of 100, with an exponential function between $8.6D$ (sponge inner) and $12.9D$ (sponge outer), as outlined in Fig. 7. Both the increase in voxel size and the sponge region have been used to mitigate reflections of acoustics waves at the domain boundaries.

To impose a pressure rise across the fan at maximum efficiency, a thin and acoustically absorbing wall has been added to the computational domain only at maximum efficiency. The pressure rise has been set by initializing the flow on the suction side of the domain with a static pressure equal to the difference between the ambient pressure and the pressure rise, as done in a previous work by the authors [17].

The fluid domain has been discretized with a resolution of 1200 voxels per diameter in the finest VR region, leading to a grid of 360 million fine equivalent voxels. The independence of the solution from the mesh size has been already assessed by the authors in [17] for a very similar numerical setup. Approximately 0.04° per timestep have been simulated for a period of 20 fan revolutions. Data has been recorded only on the last 10, resulting in a computational cost of approximately 58000 CPU hours.

The acoustic field has been sampled directly from the simulations at each timestep on a fully circular array of 12 equally spaced far-field probes, located in the plane xy at a radius $r_1/D = 2.15$ upstream of the fan rotational axis. In

addition, the instantaneous surface pressure on the blades has been sampled with a frequency of 48 kHz. Thereafter, the surface pressure is used as input to the solid formulation of the FWH analogy in PowerFLOW [42]. The spectral content of both the direct and propagated acoustic signals has been computed through the Welch averaging algorithm [43] with 4 Hamming windows and 50% of overlap, resulting in a frequency resolution of 11 Hz.

VI. Results

A. Aerodynamics

Firstly, the model capability of predicting the mean loading on the blades is assessed. Figs. 8a and 8b show the derivatives of the thrust and torque spanwise distribution on one blade for the free blowing operating condition respectively. The spanwise location r has been made dimensionless with the tip radius R. The thrust (Fig. 8a) is overpredicted by the BEMT for $r/R \geq 0.8$ due to the presence of flow separation on the blade pressure side [17] that is not considered in the model. The torque (Fig. 8b) shows instead a systematic slight underprediction by the BEMT, which becomes higher for $r/R \geq 0.9$. Nevertheless, the error on the integral value of both thrust and torque is under 10%, that can be considered acceptable.

The same analysis is conducted at maximum efficiency. It is seen that both thrust (Fig. 8c) and torque (Fig. 8d) are slightly underestimated by the BEMT. However, the overprediction at the tip is not seen in this case, confirming that this operating condition closer to the design point does not have flow separation on the pressure side, and since the error on the integral value of both quantities is under 10% as well, the modification in the BEMT model to account for the presence of a non-zero pressure rise seems acceptable and physically consistent.

The velocity reconstruction procedure at the blade trailing-edge is assessed by comparing the upwash velocity azimuthal Fourier Transform $\tilde{v}(w, r)$ obtained with the analytical model against the same quantity sampled from the time-averaged flow field of the LBM simulations in the fixed reference frame. Figure 9 shows the upwash velocity azimuthal Fourier Transform for the EB/EV (Fig. 9a) and UB/UV (Fig. 9b) configurations at free blowing evaluated at the blade trailing-edge. The quantity has been made dimensionless with the tip velocity v_{tip}. The horizontal axis represents the mode order (i.e., the harmonic of the fan rotational frequency) and is normalized by the number of blades, while the vertical axis represents the spanwise coordinate made dimensionless with the rotor tip radius. It is seen that the analytical velocity reconstruction procedure results in sufficiently accurate results both in frequency and space. This occurs consistently between the EB/EV and UB/UV configurations giving confidence that the blade loading harmonics are well computed. As a matter of fact, a previous work by the author [19] demonstrated that the Sears' model provides sufficient accuracy to model this kind of loading fluctuations on the blades as long as the input time-averaged flow field is closely accurate.

The same analysis is then conducted at the vane leading-edge to ensure that also the loading fluctuations on the stator surface are properly computed with the analytical approach. Figure 11 shows the upwash velocity azimuthal Fourier Transform for the EB/EV (Fig. 11a) and UB/UV (Fig. 11b) configurations at free blowing evaluated at the vane leading-edge. The corresponding quantity in the LBM simulations has been sampled in the rotating reference frame. The EB/EV configuration (Fig. 11a) shows that the analytical model can correctly predict the location and spanwise evolution of the main fluctuations but does not consider the presence of low frequency fluctuations that are instead seen in the LBM flow field. This is attributed to the presence of viscous vortical structures in the LBM flow field that are not considered by the potential flow calculation in the analytical model. However, it is expected that their contribution will be found in the broadband leading-edge noise calculation outlined in Section IVB. The UB/UV configuration (Fig. 11b) shows similar behavior except for the fact that a slight underestimation of the amplitude is seen around $|w/B| = 1$.

At max efficiency the same conclusions can be drawn for both the blade trailing-edge (Fig. 10) and vane leading-edge (Fig. 12). This validates the analytical velocity reconstruction approach independently of the operating condition.

B. Far-field noise

Finally, the model capability to predict the far-field acoustics is assessed. Figure 13 shows the pressure fluctuations in the far-field, at $r_1/D = 2.15$ and $\varphi = 0$ for both the EB/EV (Fig. 13a) and UB/UV (Fig. 13b) configurations at free blowing. The signal from the LBM simulation has been sampled directly from the flow field. The broadband noise is correctly computed by the analytical model within few dBs for both the EB/EV and UB/UV configurations. The EB/EV configuration (Fig. 13a) is characterized by few prominent tones, which are seen at $f/BPF = 1$ and $f/BPF = V/B$. The latter one represents the characteristic frequency of rotor-stator interaction when the rotor-stator axial spacing is

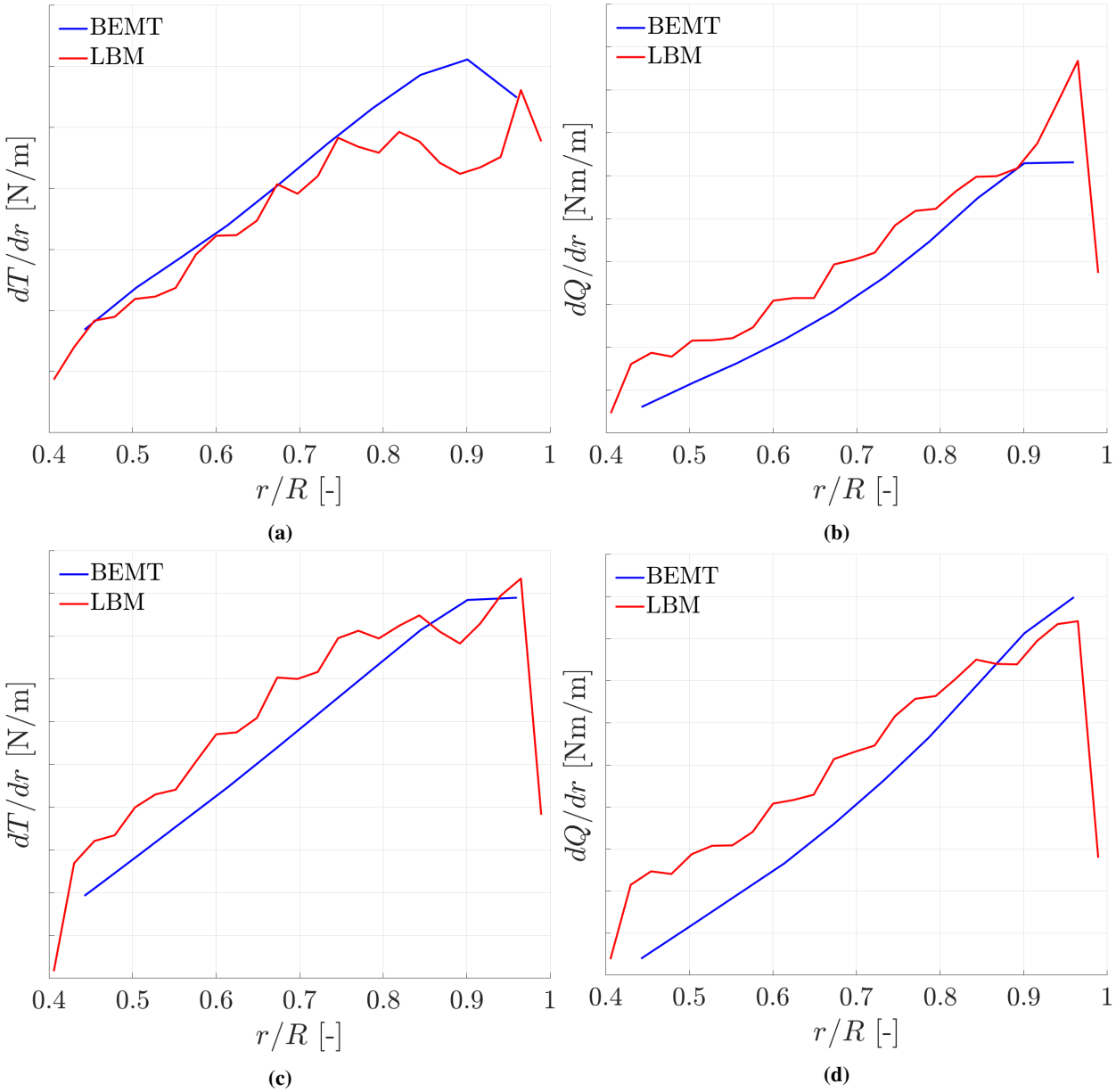

Fig. 8 Spanwise distribution of thrust and torque derivatives on one blade sampled from the LBM and computed with the BEMT model. (a): Thrust (free blowing). (b): Torque (free blowing). (c): Thrust (max efficiency). (d): Torque (max efficiency)

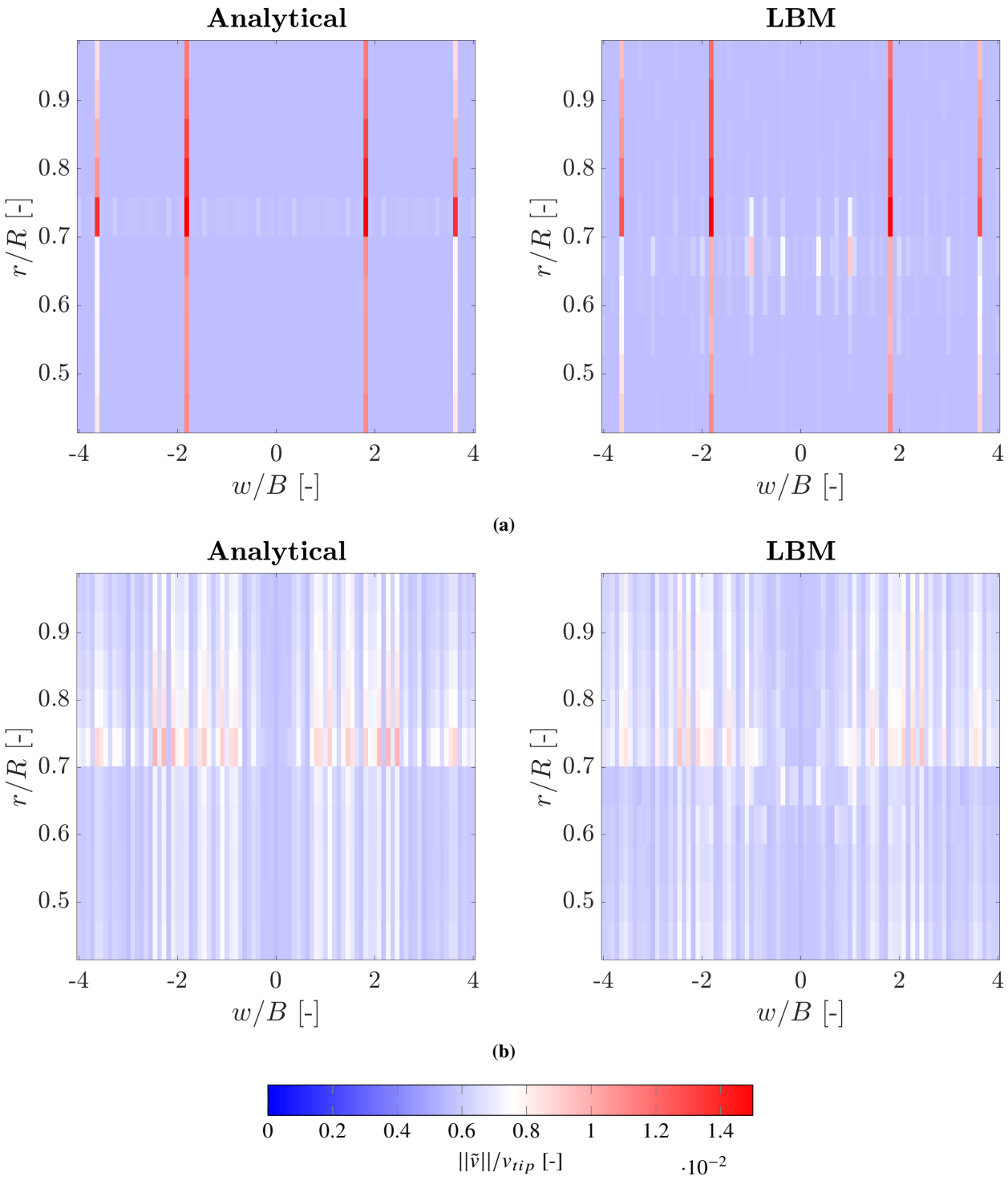

Fig. 9 Azimuthal Fourier Transform of the time-averaged upwash velocity at the blade trailing-edge at free blowing. (a): EB/EV. (b): UB/UV.

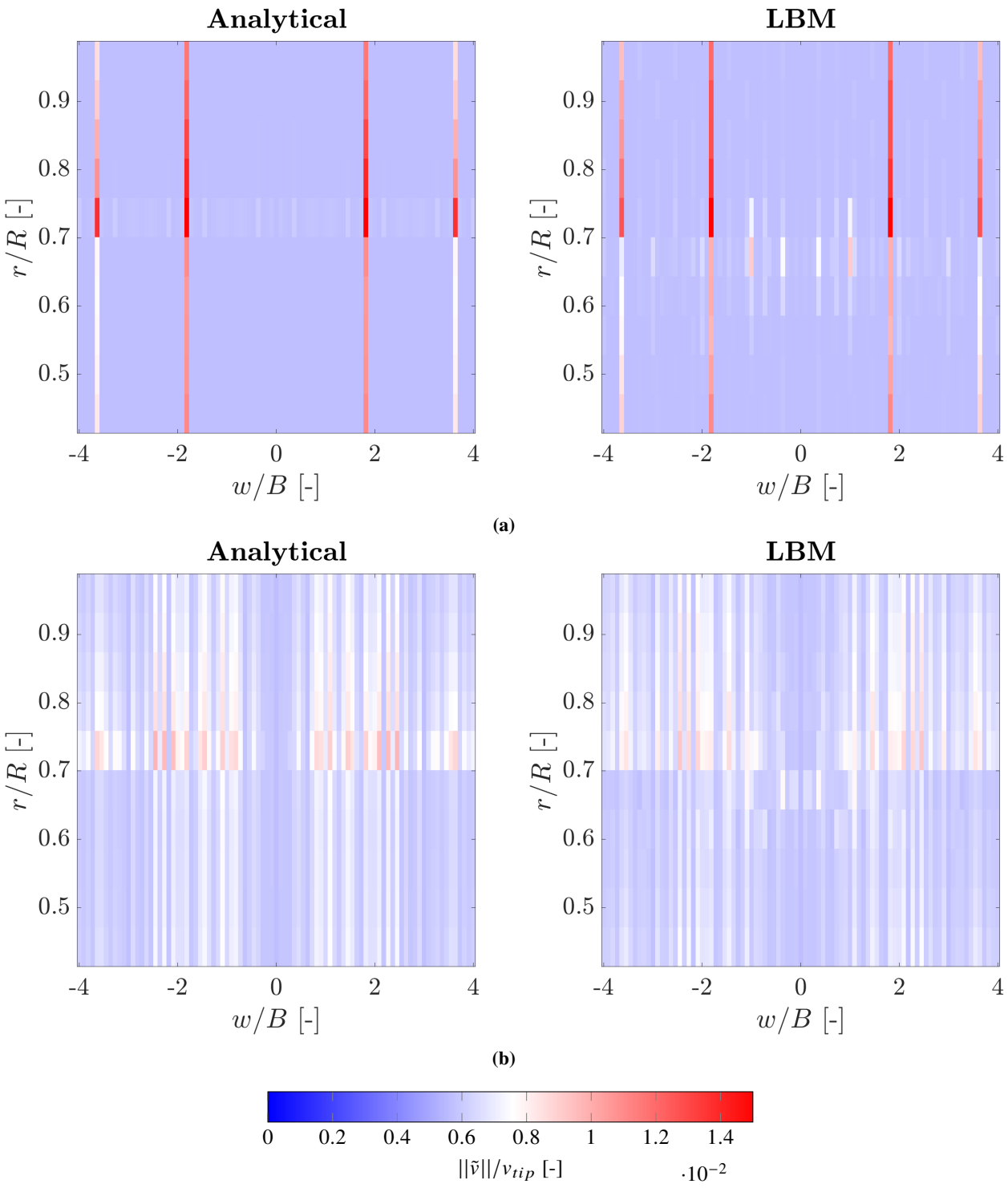

Fig. 10 Azimuthal Fourier Transform of the time-averaged upwash velocity at the blade trailing-edge at max efficiency. (a): EB/EV. (b): UB/UV.

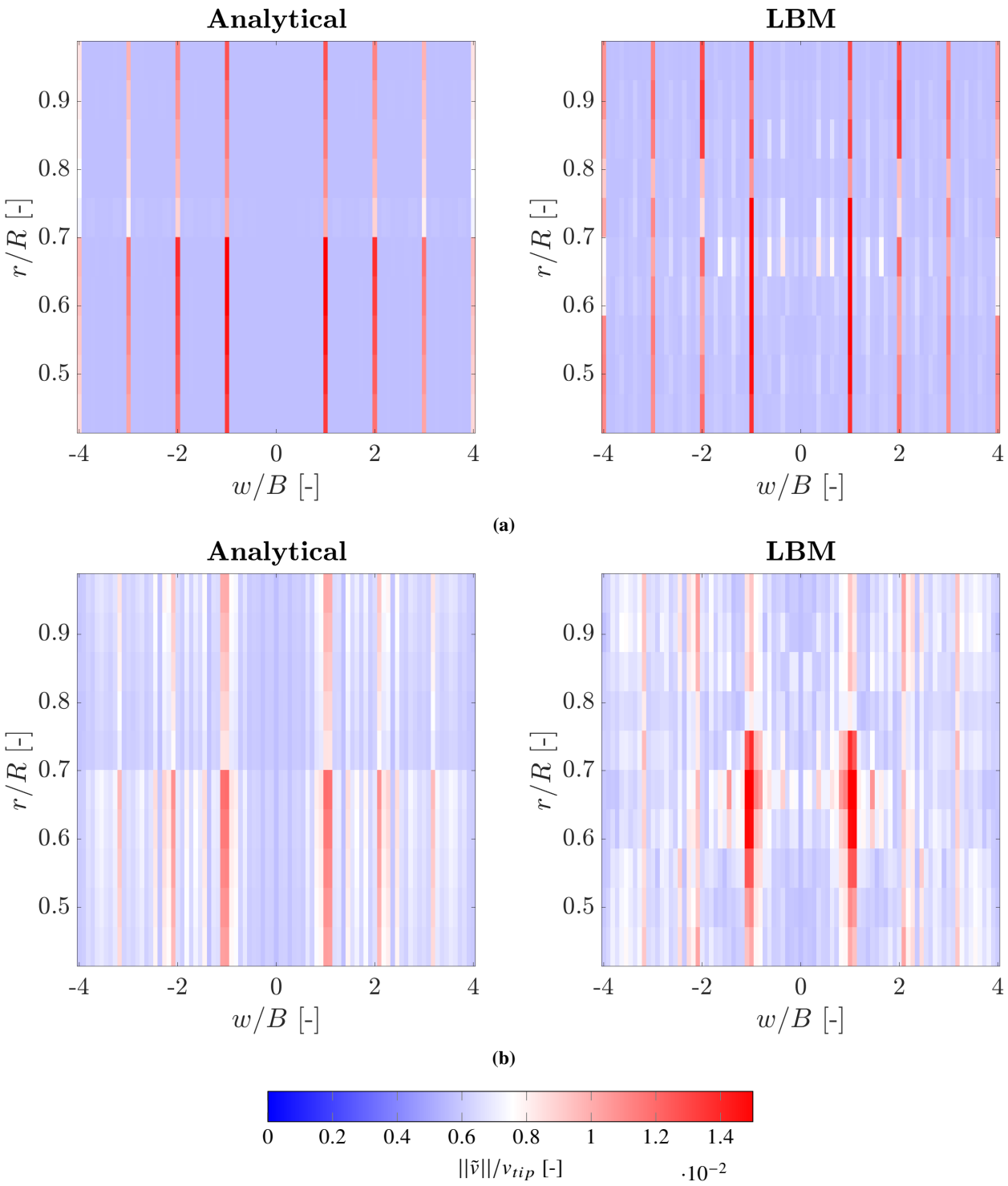

Fig. 11 Azimuthal Fourier Transform of the time-averaged upwash velocity at the vane leading-edge at free blowing. (a): EB/EV. (b): UB/UV.

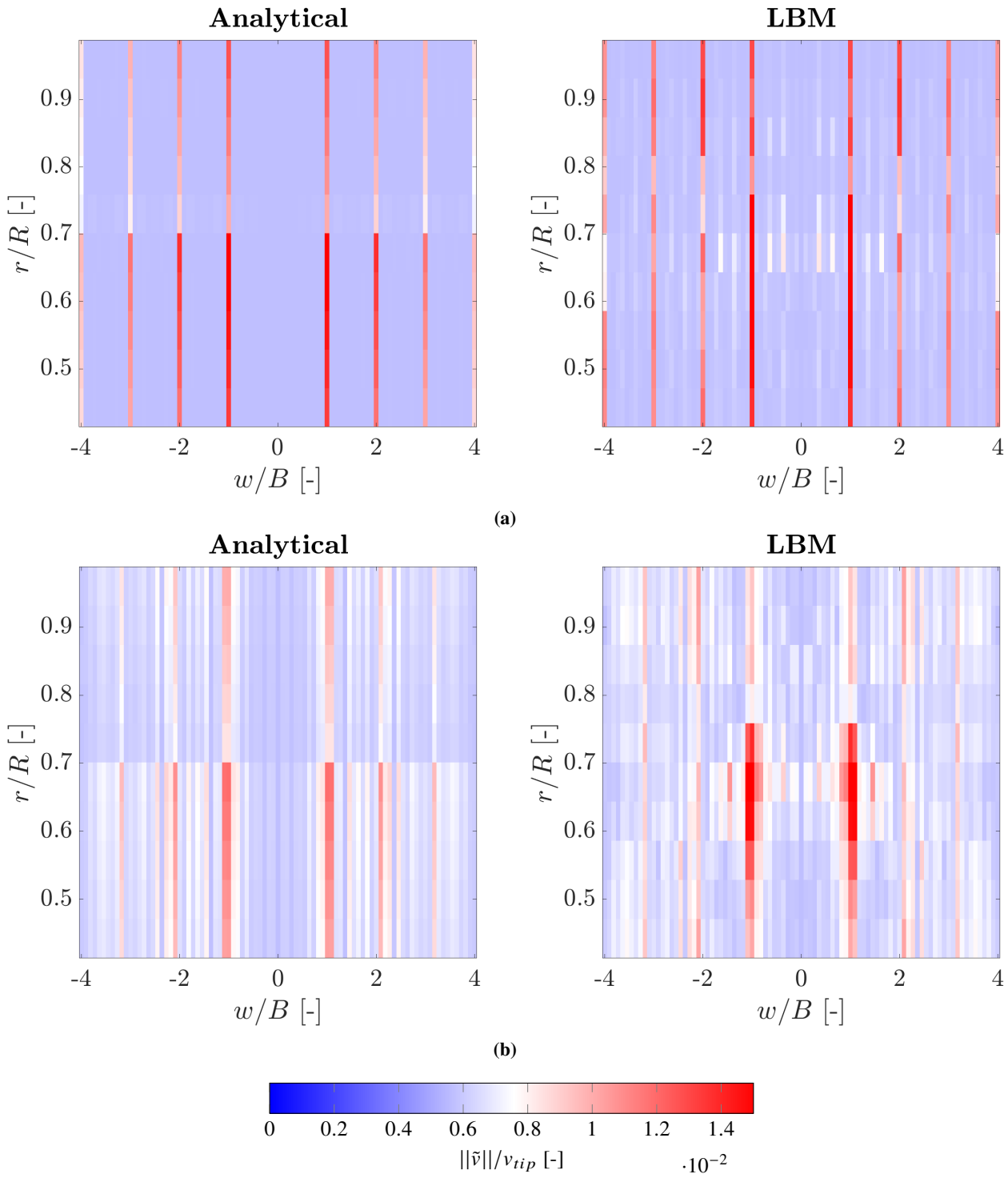

Fig. 12 Azimuthal Fourier Transform of the time-averaged upwash velocity at the vane leading-edge at max efficiency. (a): EB/EV. (b): UB/UV.

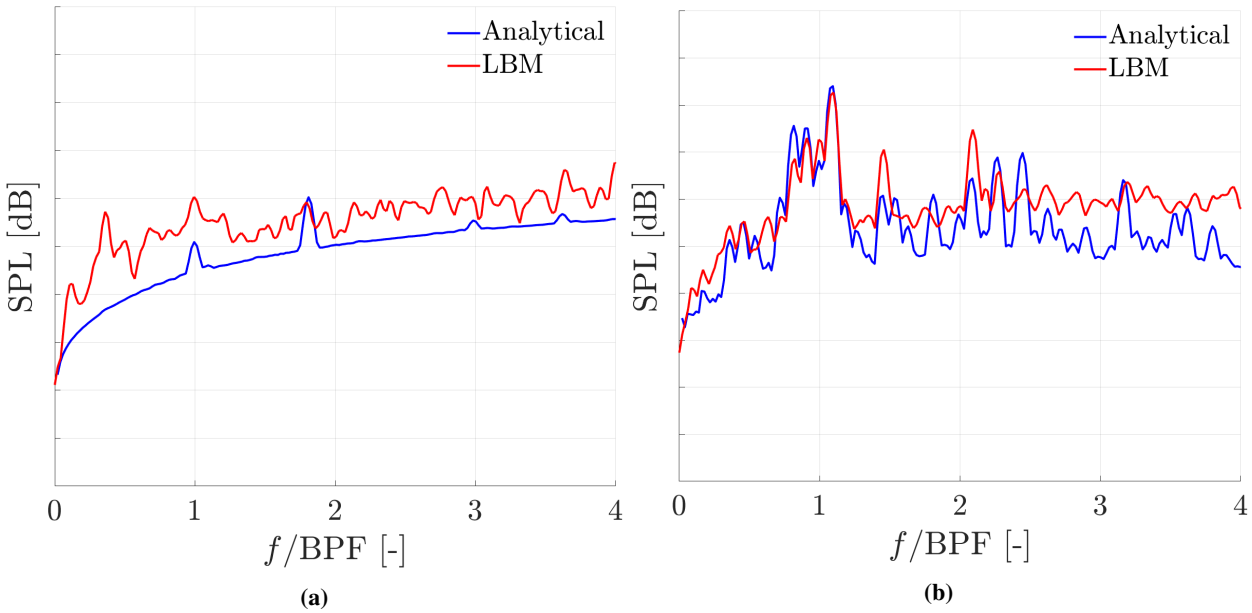

Fig. 13 Pressure fluctuations in dB at $r_1/D = 2.15$ and $\varphi = 0$ at free blowing. (a): EB/EV. (b): UB/UV.

sufficiently small. On the contrary, the UB/UV configuration (Fig. 13b) shows the presence of several tones, both at the BPF and harmonics and at subharmonic frequencies that are predicted by the analytical model within 5 dB with respect to the LBM signal.

When the engine cooling fan operates at max efficiency (Fig. 14), the tones are well computed by the analytical model but the broadband is underestimated by a higher amount with respect to the free blowing condition. As a matter of fact, a previous work by the author [17] showed that the max efficiency operating condition is often characterized by an additional noise source on the rotor, represented by its interaction with a backflow recirculation vortex that comes from the tip clearance, due to the presence of a non-zero pressure rise across the fan. Therefore, this noise source should be included as a leading-edge noise contribution to the rotor broadband noise.

Moreover, the analytical model capability to predict the variations in SPL between the UB/UV and EB/EV configurations at discrete frequencies is assessed. Figure 15 shows the ΔSPL between UB/UV and EB/EV configurations for a far-field probe located at $r_1/D = 2.15$ and $\varphi = 0$ for the free blowing (Fig. 15a) and max efficiency (Fig. 15b) operating points. The SPL has been integrated in a frequency band of width $\Delta f/\Omega = 1$ and centred at frequencies multiple of Ω. The model correctly computes the ΔSPL up to the first BPF harmonic while fails at higher frequencies for the free blowing case (Fig. 15a). This is attributed to the additional contribution of the flow separation on the pressure side that is not considered in the model. However, it should be noted that the model still predicts well the fact that the ΔSPL decreases from the second to the third harmonic of the BPF with the correct slope. At maximum efficiency (Fig. 15b) the model overestimates the ΔSPL up to the first BPF harmonics, even though the sign of the quantity is correctly computed. At the second BPF harmonic the model fails to predict the ΔSPL while at the third BPF harmonics the value compares well with the LBM signal. The discrepancies seen in this case are attributed to the lack of the rotor-backflow interaction noise source in the analytical model. Nevertheless, at both free blowing and max efficiency the ΔSPL frequency trend predicted by the analytical model compares well with the LBM signal and is considered physically consistent for further applications of the model.

VII. Conclusions

An analytical model for predicting both tonal and broadband noise from low-speed axial fans coupled with a stator is presented. The model accounts for the main dipolar sources of fan noise, including unsteady loading on both rotor and stator blades, as well as trailing-edge and leading-edge broadband contributions. Its implementation requires only geometrical and operational input parameters, making it suitable for early stage design optimization when high-fidelity simulations are computationally prohibitive.

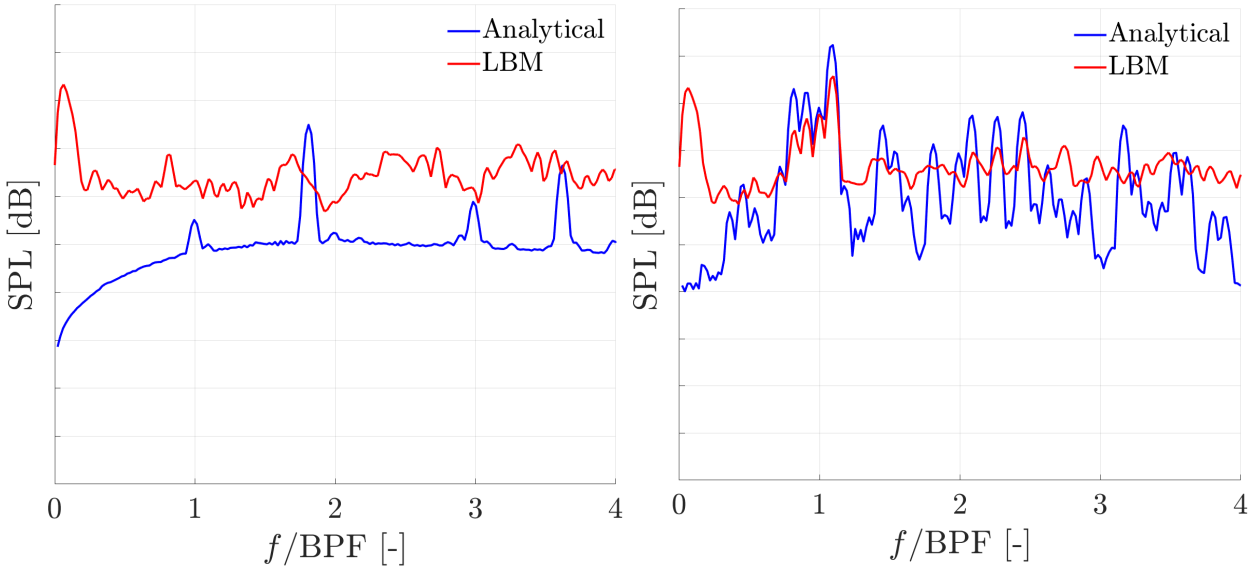

Fig. 14 Pressure fluctuations in dB at $r_1/D = 2.15$ and $\varphi = 0$ at max efficiency. (a): EB/EV. (b): UB/UV.

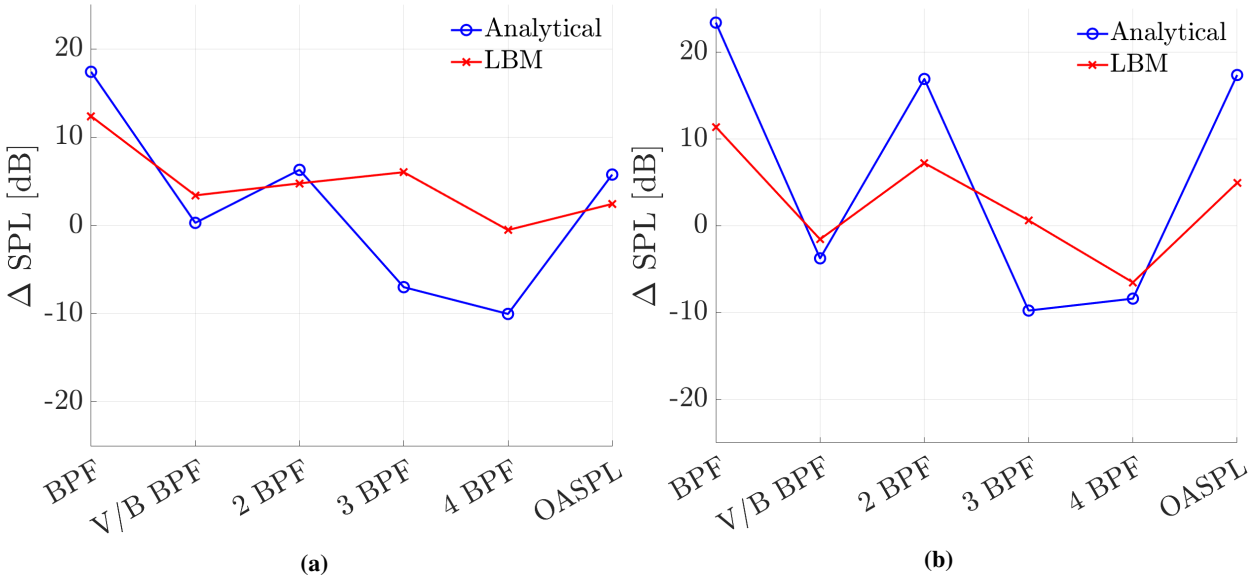

Fig. 15 Narrowband SPL difference between the UB/UV and EB/EV configurations for a far-field probe located at $r_1/D = 2.15$ and $\varphi = 0$. (a): Free blowing. (b): Max efficiency.

The model predictions are validated against high-fidelity lattice-Boltzmann numerical simulations for both evenly and unevenly spaced rotor-stator configurations at free blowing and maximum efficiency operating conditions. The results demonstrates that the analytical model is capable of accurately reproducing the mean aerodynamic loading and the associated tonal noise content, including the effect of uneven spacing on the discrete frequency peaks. The broadband noise levels are also well predicted at free blowing, while a systematic underestimation is observed at maximum efficiency due to additional rotor-backflow interaction mechanisms not yet included in the model.

Overall, the analytical framework captures the main physical mechanisms governing tonal and broadband noise generation in rotor-stator systems with satisfactory quantitative agreement and extremely low computational cost. The results highlight its potential as a predictive and design-oriented tool for parametric investigations and optimization of cooling fans. The primary limitations of the present framework are the lack of a semi-empirical model to compute the backflow-rotor interaction broadband noise and the inclusion of eventual contributions to both tonal and broadband noise due to the presence of a heat exchanger upstream of the fan.

Future work will focus on extending the model to include the contribution of the radiator presence and the backflow-rotor interaction broadband noise, as well as coupling it with an optimization algorithm to design quieter and efficient fans in the future.

References

[1] Moreau, S., and Roger, M., "Advanced noise modeling for future propulsion systems," *International Journal of Aeroacoustics*, Vol. 17, No. 6-8, 2018, pp. 576–599. https://doi.org/10.1177/1475472X18789005.

[2] Díaz, A. K. M., Fernández, O. J. M., Marigorta, E. B., and Morros, C. S., "Numerical prediction of tonal noise generation in an inlet vaned low-speed axial fan using a hybrid aeroacoustic approach," *Proceedings of the Institution of Mechanical Engineers, Part C: Journal of Mechanical Engineering Science*, Vol. 223, No. 9, 2009, pp. 2081–2098. https://doi.org/10.1243/09544062JMES1426.

[3] Sharland, I., "Sources of noise in axial flow fans," *Journal of Sound and Vibration*, Vol. 1, No. 3, 1964, pp. 302–322.

[4] Blake, W. K., *Mechanics of Flow-Induced Sound and Vibration Volume 2: Complex Flow-Structure Interactions*, Elsevier, 2017. https://doi.org/10.1016/B978-0-12-809274-3.00007-6.

[5] Vella, E., Gojon, R., Parisot-Dupuis, H., Doué, N., Jardin, T., and Roger, M., "Mutual Interaction Noise in Rotor-Beam Configuration," *30th AIAA/CEAS Aeroacoustics Conference*, American Institute of Aeronautics and Astronautics, 2024. https://doi.org/10.2514/6.2024-3318.

[6] Sears, W. R., "Some Aspects of Non-Stationary Airfoil Theory and Its Practical Application," *Journal of the Aeronautical Sciences*, Vol. 8, No. 3, 1941, pp. 104–108. https://doi.org/10.2514/8.10655.

[7] Hanson, D. B., and Parzych, D. J., "Theory for noise of propellers in angular inflow with parametric studies and experimental verification," Tech. rep., NASA. Lewis Research Center, 1993.

[8] Sanjose, M., Pestana, M., Moreau, S., and Roger, M., "Influence and modeling of OGV heterogeneity," *22nd AIAA/CEAS Aeroacoustics Conference*, American Institute of Aeronautics and Astronautics, Lyon, France, 2016. https://doi.org/10.2514/6.2016-2881.

[9] Sanjosé, M., Moreau, S., Pestana, M., and Roger, M., "Effect of Weak Outlet-Guide-Vane Heterogeneity on Rotor–Stator Tonal Noise," *AIAA Journal*, Vol. 55, No. 10, 2017, pp. 3440–3457. https://doi.org/10.2514/1.J055525.

[10] Parry, A. B., "Theoretical prediction of counter-rotating propeller noise," Ph.D. thesis, University of Leeds, 1988.

[11] Sanjosé, M., and Moreau, S., "Fast and accurate analytical modeling of broadband noise for a low-speed fan," *The Journal of the Acoustical Society of America*, Vol. 143, No. 5, 2018, pp. 3103–3113. https://doi.org/10.1121/1.5038265.

[12] Amiet, R. K., *Noise produced by turbulent flow into a rotor: theory manual for noise calculation*, National Aeronautics and Space Administration, Langley Research Center, 1989.

[13] Dieste, M., and Gabard, G., "Random particle methods applied to broadband fan interaction noise," *Journal of Computational Physics*, Vol. 231, No. 24, 2012, pp. 8133–8151.

[14] Caro, S., and Moreau, S., "Aeroacoustic modelling of low pressure axial flow fans," *6th Aeroacoustics Conference and Exhibit*, American Institute of Aeronautics and Astronautics, Lahaina,HI,U.S.A., 2000. https://doi.org/10.2514/6.2000-2094.

[15] Coutty, B., and Moreau, S., "Aeroacoustic modeling of an automotive engine cooling module," *26th International Congress on Noise and Vibration, paper*, Vol. 525, 2019.

[16] Arroyo Ramo, A., Alguacil, A., Bauerheim, M., Moreau, S., and Jacob, M. C., "Artificial Neural Networks Prediction of Wall-Pressure Spectrum," *30th AIAA/CEAS Aeroacoustics Conference (2024)*, 2024, p. 3140.

[17] Bellelli, F., Arina, R., and Avallone, F., "On the impact of operating condition and testing environment on the noise sources in an industrial engine cooling fan," *Applied Acoustics*, Vol. 227, 2025, p. 110252. https://doi.org/10.1016/j.apacoust.2024.110252.

[18] Cattanei, A., Mazzocut Zecchin, F., Di Pasquali, A., and Lazari, A., "Effect of the uneven blade spacing on the noise annoyance of axial-flow fans and side channel blowers," *Applied Acoustics*, Vol. 177, 2021, p. 107924. https://doi.org/10.1016/j.apacoust.2021.107924.

[19] Bellelli, F., Arina, R., , Moreau, S., and Avallone, F., "Analytical model for predicting rotor-stator interaction tonal noise in low-speed axial fans," *InterNoise 2025*, 2025.

[20] Lowson, M., "Theoretical Analysis of Compressor Noise," *Proceedings of the Royal Society of London. Series A, Mathematical and Physical Sciences*, 1970.

[21] Lowson, M., "The Sound Field for Singularities in Motion," *Proceedings of the Royal Society of London. Series A, Mathematical and Physical Sciences*, 1965.

[22] Ffowcs Williams, J., and Hawkings, D., "Sound Generation by Turbulence and Surfaces in Arbitrary Motion," *Philosophical Transactions of the Royal Society of London. Series A, Mathematical and Physical Sciences*, Vol. 264, No. 1151, 1969, pp. 321–342.

[23] Drela, M., "XFOIL: An Analysis and Design System for Low Reynolds Number Airfoils," *Low Reynolds Number Aerodynamics*, 1989.

[24] Amiet, R. K., "Compressibility Effects in Unsteady Thin-Airfoil Theory," *AIAA Journal*, Vol. 12, No. 2, 1974, pp. 252–255. https://doi.org/10.2514/3.49212.

[25] Goldstein, M. E., and Atassi, H., "A complete second-order theory for the unsteady flow about an airfoil due to a periodic gust," *Journal of Fluid Mechanics*, Vol. 74, No. 4, 1976, pp. 741–765. https://doi.org/10.1017/S0022112076002036.

[26] Atassi, H. M., "The Sears problem for a lifting airfoil revisited - new results," *Journal of Fluid Mechanics*, Vol. 141, 1984, pp. 109–122. https://doi.org/10.1017/S0022112084000768.

[27] Roger, M., and Carazo, A., "Blade-Geometry Considerations in Analytical Gust-Airfoil Interaction Noise Models," *16th AIAA/CEAS Aeroacoustics Conference*, American Institute of Aeronautics and Astronautics, Stockholm, Sweden, 2010. https://doi.org/10.2514/6.2010-3799.

[28] Baddoo, P. J., and Ayton, L. J., "Potential flow through a cascade of aerofoils: direct and inverse problems," *Proceedings of the Royal Society A: Mathematical, Physical and Engineering Sciences*, Vol. 474, No. 2217, 2018, p. 20180065. https://doi.org/10.1098/rspa.2018.0065.

[29] Roger, M., and Moreau, S., "Back-scattering correction and further extensions of Amiet's trailing-edge noise model. Part 1: theory," *Journal of Sound and vibration*, Vol. 286, No. 3, 2005, pp. 477–506.

[30] Sinayoko, S., Kingan, M., and Agarwal, A., "On the effect of acceleration on trailing edge noise radiation from rotating blades," *19th AIAA/CEAS Aeroacoustics Conference*, American Institute of Aeronautics and Astronautics, Berlin, Germany, 2013. https://doi.org/10.2514/6.2013-2287.

[31] Sinayoko, S., Kingan, M., and Agarwal, A., "Trailing edge noise theory for rotating blades in uniform flow," *Proceedings of the Royal Society A: Mathematical, Physical and Engineering Sciences*, Vol. 469, No. 2157, 2013, p. 20130065. https://doi.org/10.1098/rspa.2013.0065.

[32] Kamruzzaman, M., Bekiropoulos, D., Lutz, T., Würz, W., and Krämer, E., "A semi-empirical surface pressure spectrum model for airfoil trailing-edge noise prediction," *International journal of aeroacoustics*, Vol. 14, No. 5-6, 2015, pp. 833–882.

[33] Goody, M., "Empirical spectral model of surface pressure fluctuations," *AIAA journal*, Vol. 42, No. 9, 2004, pp. 1788–1794.

[34] Corcos, G., "The structure of the turbulent pressure field in boundary-layer flows," *Journal of Fluid Mechanics*, Vol. 18, No. 3, 1964, pp. 353–378.

[35] Von Karman, T., "Progress in the statistical theory of turbulence," *Proceedings of the National Academy of Sciences*, Vol. 34, No. 11, 1948, pp. 530–539.

[36] Meier zu Ummeln, R., and Moreau, A., "Estimation of turbulence in fan-rotor wakes for broadband noise prediction during acoustic preliminary design," *AIAA Aviation 2020 Forum*, 2020, p. 2566.

[37] He, X., and Luo, L.-S., "Theory of the lattice Boltzmann method: From the Boltzmann equation to the lattice Boltzmann equation," *Phys. Rev. E Stat. Phys. Plasmas Fluids Relat. Interdiscip. Topics*, Vol. 56, No. 6, 1997, pp. 6811–6817.

[38] Chen, H., Kandasamy, S., Orszag, S., Shock, R., Succi, S., and Yakhot, V., "Extended Boltzmann kinetic equation for turbulent flows," *Science*, Vol. 301, No. 5633, 2003, pp. 633–636.

[39] Launder, B., and Spalding, D., "The numerical computation of turbulent flows," *Comput. Methods Appl. Mech. Eng.*, Vol. 3, No. 2, 1974, pp. 269–289.

[40] Teixeira, C. M., "Incorporating turbulence models into the Lattice-Boltzmann method," *Int. J. Mod. Phys. C.*, Vol. 09, No. 08, 1998, pp. 1159–1175.

[41] Avallone, F., Ragni, D., and Casalino, D., "On the effect of the tip-clearance ratio on the aeroacoustics of a diffuser-augmented wind turbine," *Renewable Energy*, Vol. 152, 2020, pp. 1317–1327.

[42] Farassat, F., and Succi, G. P., "The prediction of helicopter rotor discrete frequency noise," *In: American Helicopter Society*, 1982, pp. 497–507.

[43] Welch, P., "The use of fast Fourier transform for the estimation of power spectra: A method based on time averaging over short, modified periodograms," *IEEE Trans. Audio Electroacoust.*, Vol. 15, No. 2, 1967, pp. 70–73.